



The First Flight of the Marshall Grazing Incidence X-Ray Spectrometer (MaGIXS)

Sabrina L. Savage¹ , Amy R. Winebarger¹ , Ken Kobayashi¹ , P. S. Athiray^{1,2} , Dyana Beabout¹, Leon Golub³ , Robert W. Walsh⁴ , Brent Beabout¹, Stephen Bradshaw⁵ , Alexander R. Brucoleri⁶ , Patrick R. Champey¹ , Peter Cheimets³, Jonathan Cirtain⁷, Edward E. DeLuca³ , Giulio Del Zanna⁸ , Jaroslav Dudík⁹ , Anthony Guillory¹, Harlan Haight¹, Ralf K. Heilmann¹⁰ , Edward Hertz³ , William Hogue¹, Jeffery Kegley¹, Jeffery Kolodziejczak¹, Chad Madsen³ , Helen Mason⁸ , David E. McKenzie¹ , Jagan Ranganathan¹, Katharine K. Reeves³ , Bryan Robertson¹, Mark L. Schattenburg¹⁰ , Jorg Scholvin⁶, Richard Siler¹, Paola Testa³ , Genevieve D. Vigil¹ , Harry P. Warren¹¹ , Benjamin Watkinson⁴, Bruce Weddendorf¹², and Ernest Wright¹

¹ NASA Marshall Space Flight Center, Huntsville, AL 35812, USA; sabrina.savage@nasa.gov

² Center for Space Plasma and Aeronomic Research, University of Alabama Huntsville, Huntsville, AL, 35812, USA

³ Center for Astrophysics | Harvard & Smithsonian, Cambridge, MA 02138, USA

⁴ University of Central Lancashire, Preston, PR1 2HE, UK

⁵ Department of Physics and Astronomy (MS 108), Rice University, 6100 Main Street, Houston, TX 77005, USA

⁶ Izentis LLC, Cambridge, MA 02139, USA

⁷ BWX Technologies, Lynchburg, VA 24504, USA

⁸ DAMTP, Centre for Mathematical Sciences, University of Cambridge, Wilberforce Road, Cambridge CB3, UK

⁹ Astronomical Institute, Czech Academy of Sciences, Fričova 298, 251 65 Ondřejov, Czech Republic

¹⁰ Massachusetts Institute of Technology, Cambridge, MA 02139, USA

¹¹ Space Science Division, Naval Research Laboratory, Washington, DC 20375, USA

¹² Weddendorf Design, Inc., Huntsville, AL 35803, USA

Received 2022 December 8; revised 2023 January 24; accepted 2023 February 7; published 2023 March 13

Abstract

The Marshall Grazing Incidence X-ray Spectrometer (MaGIXS) sounding rocket experiment launched on 2021 July 30 from the White Sands Missile Range in New Mexico. MaGIXS is a unique solar observing telescope developed to capture X-ray spectral images of coronal active regions in the 6–24 Å wavelength range. Its novel design takes advantage of recent technological advances related to fabricating and optimizing X-ray optical systems, as well as breakthroughs in inversion methodologies necessary to create spectrally pure maps from overlapping spectral images. MaGIXS is the first instrument of its kind to provide spatially resolved soft X-ray spectra across a wide field of view. The plasma diagnostics available in this spectral regime make this instrument a powerful tool for probing solar coronal heating. This paper presents details from the first MaGIXS flight, the captured observations, the data processing and inversion techniques, and the first science results.

Unified Astronomy Thesaurus concepts: [Spectroscopy \(1558\)](#); [Solar active regions \(1974\)](#); [Solar x-ray emission \(1536\)](#); [Solar coronal heating \(1989\)](#); [Solar corona \(1483\)](#); [Active solar corona \(1988\)](#); [Solar atmosphere \(1477\)](#)

1. Introduction

X-ray spectroscopy provides unique capabilities for answering fundamental questions in solar physics (Del Zanna et al. 2021a; Young 2021). The X-ray regime is dominated by emission lines formed at high temperatures, with untapped potential to yield insights into basic physical processes of the Sun and stars that are not accessible by any other means. The Marshall Grazing Incidence X-ray Spectrometer (MaGIXS) is a sounding rocket instrument developed as a pathfinder to acquire the first-ever spatially and spectrally resolved images discriminating between coronal active region structures in X-rays, without the restriction of a slit. The MaGIXS wavelength range (6–24 Å) with available spectral lines is shown in Figure 1. Herein, we refer to these wavelengths as soft X-rays (SXR), as compared to those observed by hard X-ray detectors such as the Reuven Ramaty High Energy Solar Spectroscopic Imager (RHESSI); however, it should be noted that this classification varies (e.g., Del Zanna et al. 2021a).

For the last 20 yr, solar astrophysics has heavily relied on measurements of coronal plasma using extreme ultraviolet (EUV), ultraviolet (UV), or white light instrumentation along with broadband X-ray imaging. Significant progress has been made using these resources to discern elemental composition and fractionation (e.g., Schmelz et al. 2012; Laming 2015; Brooks et al. 2017; Stansby et al. 2020), as well as properties of relatively cool plasma such as temperature structure (e.g., Reale et al. 2007; Tripathi et al. 2009; Del Zanna 2011; Warren et al. 2012; Parenti et al. 2017; Brooks 2019; Testa & Reale 2020) and densities (e.g., Watanabe et al. 2009; Young et al. 2009; Gupta et al. 2015; Chitta et al. 2016; Dudík et al. 2021). However, there remains limited access (Winebarger et al. 2012) to key spectral diagnostics for various structures and events in the corona, in particular at high temperatures, that would build upon and broaden these efforts. As there has been hardly any SXR imaging spectroscopy of the solar corona since the Orbiting Solar Observatory (OSO) era (1962–1975), besides the Bragg Flat Crystal Spectrometer (FCS) instrument on the Solar Maximum Mission (SMM, 1980–1989), which had relatively poor spatial resolution, there is a massive well of untapped potential for future discovery. The first flight of MaGIXS, occurring after a decade of technology and



Original content from this work may be used under the terms of the [Creative Commons Attribution 4.0 licence](#). Any further distribution of this work must maintain attribution to the author(s) and the title of the work, journal citation and DOI.

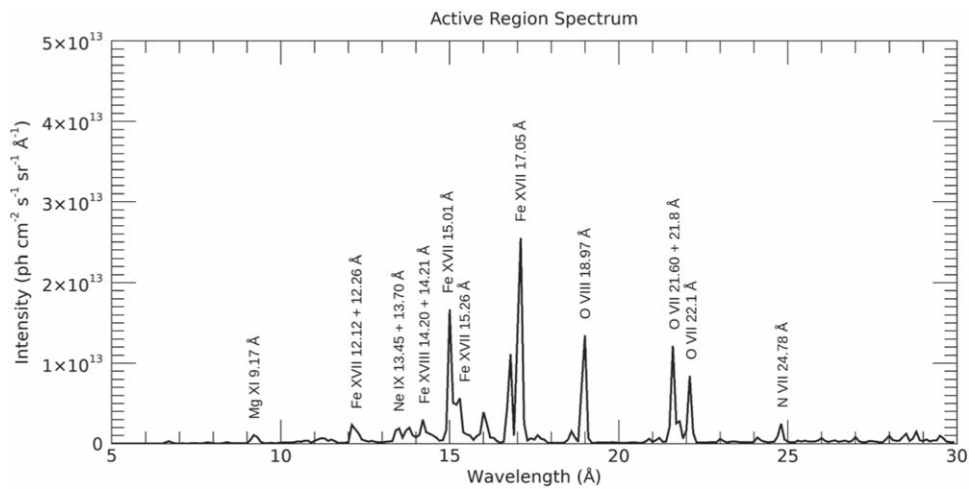


Figure 1. The MaGIXS wavelength range (6–24 Å) and spectrum with the strongest spectral lines identified, derived from CHIANTI using an active region differential emission measure.

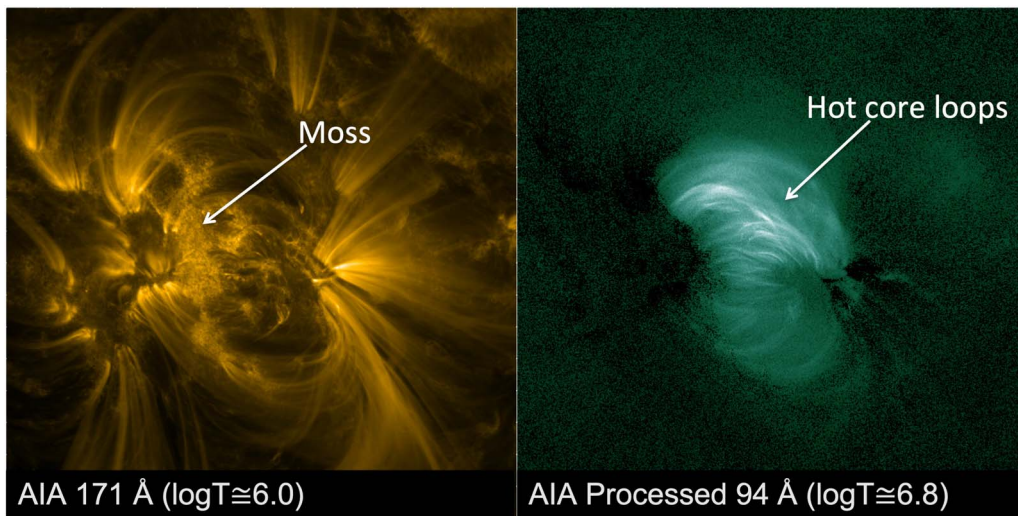


Figure 2. (Left) Active Region 11339 observed 2011 November 10. The footpoints of the high-temperature loops form the reticulated emission in the SDO/AIA Fe IX/X 171 Å image. (Right) The hot active region core is shown in the processed SDO/AIA Fe XVIII 94 Å image. The size of the image is $8' \times 8'$. The log of the approximate dominant emitting temperature is given in each image.

instrument development, demonstrates a revolutionary concept for advancing such grazing incidence imaging spectroscopy.

For a short-duration rocket flight, the overarching science goal of MaGIXS targets the frequency of heating in active region cores, an essential measurement needed to solve the elusive coronal heating problem discovered by Edlén and Grotrian in the 1930s. Two primary mechanisms are anticipated to play dominant roles in the transfer and dissipation of energy into the corona: magnetic reconnection (Parker 1983a, 1983b) and wave heating (van Ballegoijen et al. 2011, 2014). Energy released through single field-line reconnection events (i.e., nanoflares) due to forced interactions between stressed magnetic fields via photospheric motions is expected to be sporadic, short-lived, and *infrequent* (e.g., López Fuentes & Klimchuk 2010). Conversely, magnetic wave heating along these field lines would also be sporadic and short-lived, but *frequent* (Asgari-Targhi & van Ballegoijen 2012).

The heating frequency in the highest-temperature loops in the solar corona, those in the active region core, remains the most controversial. Figure 2 shows an example active region observed with the Solar Dynamics Observatory (SDO)

Atmospheric Imaging Assembly (AIA). The left panel shows the 1 MK footpoints of high-temperature loops, or “moss,” and the right panel shows the 94 Å channel emission with the cool contribution removed (following Warren et al. 2012). The remaining emission is expected to be from the Fe XVIII spectral line formed within the ~ 4 –8 MK range (Testa & Reale 2012; Reale et al. 2019; Testa & Reale 2020). Many diagnostics have attempted to glean the heating frequency from cooler (1–4 MK) observations of these hot core loops (see, for instance, Cargill 2014; Bradshaw & Viall 2016; Barnes et al. 2019, 2021); however, these are often difficult to interpret, due to contributions of overlying cool structures or the moss footpoints (e.g., Tripathi et al. 2010) and other errors (Guennou et al. 2013).

Spectral observations in the SXR regime provide the most unambiguous means of differentiating between the heating frequency cases through characteristic variations in observables. MaGIXS is designed to optimally discriminate between these competing coronal heating theories by providing SXR spectra along spatially resolved active region features—a combination that no other solar instrument offers. The unique

and powerful plasma diagnostics afforded through SXR spectral imaging to achieve this goal include measurements of

1. emission from Fe XVII–Fe XX to assess the temperature distribution above 4 MK in an active region,
2. elemental abundances of high-temperature plasma,
3. the temporal variability of high-temperature plasma (Fe XVII) at high cadence, and
4. the presence of non-Maxwellian electron distributions.

I. High-temperature, low-emission plasma: *High-frequency heating scenario*: If the frequency of energy release on a given strand¹³ is high, the plasma along that strand does not have time to cool before being reheated. As a result, the temperature and density of the strand remain relatively constant. *Low-frequency heating scenario*: If the frequency of heating events is low (i.e., the time between two heating events on a given strand is longer than the plasma’s cooling time), the plasma’s density and temperature along that strand would be dynamic and evolving. During its evolution, the temperature would be both much higher and much lower than the average temperature. Because an observed loop is almost certainly formed of many strands (e.g., Kobelski et al. 2014; Williams et al. 2020), the loop’s properties may or may not reflect this evolution. If the loop is formed of many unresolved strands, each strand being heated randomly and then evolving, the observed loop’s intensity can appear steady regardless of the dynamic nature of the plasma along a single strand (Klimchuk 2009).

One well-studied observation that can discriminate between low- and high-frequency heating in active region cores is the relative amount of high-temperature (~ 5 – 10 MK) to average temperature (~ 3 – 5 MK) plasma (e.g., Ko et al. 2009; McTiernan 2009; Reale et al. 2009; Sylwester et al. 2010; Testa et al. 2011; Miceli et al. 2012; Brosius et al. 2014; Ishikawa et al. 2014; Petralia et al. 2014; Barnes et al. 2016; Athiray et al. 2020). Athiray et al. (2019) demonstrated that the heating frequency can be easily gleaned from simple intensity ratios between spectrally pure Fe XVII, XVIII, or XIX intensities (Figure 11 therein). Further, they demonstrated that intensities from existing instruments, like Hinode’s X-Ray Telescope (XRT) or AIA, were insensitive to the heating frequency, possibly due to their broadband filter response functions. The relative variations in the responses may not have the resolution to distinguish high-temperature emission. Instead, these instruments are more sensitive to the cool slope (α) versus the hot slope (β).

The emissivity functions for key MaGIXS strong spectral lines are shown in Figure 1 of Champey et al. (2022). MaGIXS provides better high-temperature coverage and temperature discrimination than is currently available in EUV spectrometers or in EUV or X-ray imagers (see Figure 3 for examples of comparisons to Hinode’s EUV Imaging Spectrograph; EIS). The EIS instrument, which currently provides the highest-temperature spectrally pure measurements of the solar corona, is able to detect plasma with temperatures up to 4 MK very well, but in the 4–10 MK range the lines are weak and blended with other transitions (see, e.g., Del Zanna & Ishikawa 2009; Del Zanna et al. 2011).

¹³ Here, we use the term “strand” to refer to the fundamental plasma feature in the corona and the term “loop” to refer to a spatially coherent structure in an observation. A loop can consist of a single strand—or more likely, many subresolution strands.

II. Element abundances of high-temperature plasma: Early spectroscopic observations at X-ray and EUV wavelengths allowed the first measurements of the abundances of different elements in the solar corona. Unexpectedly, however, the composition of the corona did not always match the composition of the underlying photosphere (e.g., Evans & Pounds 1968; Widing & Sandlin 1968; Withbroe 1975; Parkinson 1977; Veck & Parkinson 1981). The abundances of a few elements sometimes appeared to be enhanced, while the abundances of other elements remained closer to their photospheric values, or even lower (Raymond et al. 1997). The enhanced elements, such as Fe and Si, have low first ionization potential (FIP < 10 eV), while the nonenhanced elements, such as O and Ne, have high-FIP $\gtrsim 10$ eV; see reviews by Meyer (1985), Feldman (1992), Sylwester et al. (2010), Testa (2010), Laming (2015), and Del Zanna & Mason (2018). The “FIP bias” (i.e., the enhancement ratio of low-FIP elements) is generally found to be a factor of ~ 2 – 4 .

Several studies have revealed that FIP bias of coronal structures is a consequence of the plasma’s time of confinement in coronal structures (e.g., Ugarte-Urra & Warren 2012; Del Zanna & Mason 2014; Warren 2014). Impulsively heated loops or jets have a photospheric composition (low-FIP bias), while quiescent loops have coronal abundances (high-FIP bias), thereby linking abundance measurements to the frequency of coronal heating. The MaGIXS spectral region is the most suitable to measure the FIP bias of hot plasma in the 3–10 MK range. Previous observations in this spectral region of quiescent active region cores have indicated a FIP bias of about 3 (Del Zanna & Mason 2014). Simple ratios of the strong lines listed in Table 1 provide the relative abundance diagnostics largely independent of the temperature structure of the plasma (e.g., Drake & Testa 2005; Huenemoerder et al. 2009; Testa 2010). These ratios allow for comparisons to expected abundance measurements from modeled heating frequency scenarios, and by virtue of the spatial resolution of MaGIXS, comparisons can be made between active region structures.

III. Temporal variability of high-temperature plasma: In an active region, the overlapping of many optically thin loops, possibly consisting of smaller unresolved strands (e.g., Brooks et al. 2012), complicates the identification of individual heating events. Nevertheless, statistical analysis of high-temperature light curves can provide information on the frequency of heating in an active region (e.g., Ugarte-Urra & Warren 2014). Because the light curve of an individual impulsive heating event includes a steep rise in time followed by a slower decay phase (López Fuentes & Klimchuk 2010), an impulsive heating scenario would result in significant skew in the light-curve fluctuations as a function of time. An analysis performed by Terzo et al. (2011) found a skewness in XRT active region light curves that could not be accounted for by Poisson noise alone. The lifetimes of their identified events were on the order of 100–500 s, and the XRT intensity enhancement was on the order of 20%. However, these measurements are very sensitive to the noise in the data, and the light curve identification is further complicated by the broad temperature response of the XRT filters. Additionally, the measurements by Terzo et al. (2011) were performed with the XRT Al-poly filter, which has significant contributions from cooler temperatures (Golub et al. 2007).

IV. Presence of non-Maxwellian electron distributions: Departures from a Maxwellian distribution, especially the

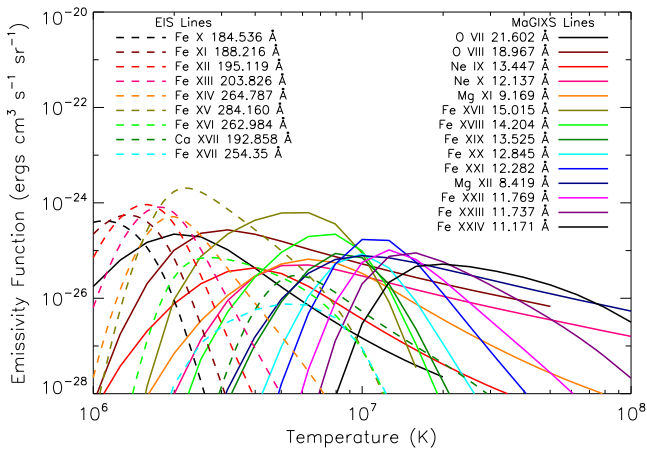


Figure 3. The emissivity functions for key MaGIXS spectral lines (solid) compared to the emissivity functions of key Hinode/EIS spectral lines (dashed). Though the EIS wavelength range does contain a few high-temperature lines, these are weak and blended and tend to be observed well only during a solar flare. The temperature range of $6.2 < \text{Log } T < 7.2$ is covered well by the MaGIXS spectral lines.

Table 1
Key Spectral Lines Appropriate for Abundance Analysis

Ion	Wavelength (Å)	Log Temperature
Mg XII	8.42 Å	6.9
Mg XI	9.16 Å	6.4
Ne X	12.13 Å	6.6
Ne IX	13.45 Å	6.2
Fe XVIII	14.21 Å	6.8
Fe XVII	15.01 Å	6.6
O VIII	18.97 Å	6.4
O VII	21.60 Å	6.3

presence of high-energy tails that would be detectable in the SXR regime, are expected to arise due to magnetic reconnection or wave-particle interactions. Quantifying the number of high-energy particles provides strong constraints on the possible coronal heating mechanisms, with the presence of non-Maxwellian distributions clearly indicating nanoflare heating. The potential of the MaGIXS instrument in this respect is discussed in Dudik et al. (2019).

Despite its clear utility, obtaining SXR spectra is considerably more difficult than for longer wavelengths, due to the challenges involved with (1) aligning grazing incidence optics with a slit and grating assembly, (2) low SXR throughput through a slit system, and (3) fabricating a grazing incidence, varied-line space grating. Alignment and throughput requirements are loosened (although not eliminated) with the use of a wide slot versus a slit, but with the added complication of obtaining overlapping spectral line images of the field of view across the detector. These resulting spectroheliogram images (also referred to as “overlappograms”) provide a wealth of information with spectra obtained across the entire field of view in a single image, but require significant advancements in deconvolution techniques in order to separate the lines.

Fortunately, great strides have been made in recent years in advancing the necessary inversion methods for other missions (e.g., the Multi-slit Solar Explorer (MUSE)) that now make it possible to extract pure spectral line images from the MaGIXS spectroheliograms (Cheung et al. 2015; Winebarger et al. 2019;

Cheung et al. 2019). MaGIXS takes advantage of these revolutionary analysis breakthroughs, along with innovative advancements in high-resolution grazing incidence mirror fabrication, optimized grating lithography, and improved camera efficiencies, to produce wide field of view SXR spectral images.

This paper provides an overview of the first MaGIXS flight, the calibration and inversion processing of the flight data, and initial results from analysis on a bright region observed by MaGIXS.

2. Instrument Overview

The MaGIXS instrument is described in detail in Champey et al. (2022). It was designed as a fully grazing incidence slit spectrograph, consisting of a Wolter-I telescope, slit, spectrometer, CCD camera, and slitjaw context imager. The optical path is illustrated in Figure 4. The spectrometer comprises a matched pair of grazing incidence parabolic mirrors, which reimages the slit, and a planar varied-line space grating. All mirrors are single, thin-shell, nickel-cobalt replicated mirrors made by NASA Marshall Space Flight Center (MSFC). The X-ray mirrors and grating are mounted on an optical bench, and they are collectively termed as the Telescope Mirror Assembly (TMA) and Spectrometer Optical Assembly (SOA) (see Champey et al. 2022). The $2k \times 2k$ CCD is operated as a $2k \times 1k$ frame-transfer device, allowing image readout concurrent with exposure. Due to the lower-than-expected throughput of the optics, as well as the recognition of the value of slot spectrographs in providing both spatial and spectral information, MaGIXS was fitted with a $12'$ -wide slot instead of the originally intended narrow slit. MaGIXS includes a “slitjaw” context imager, described in Vigliani et al. (2021).

3. Flight Overview

The first flight of MaGIXS occurred at 18:20 UT on 2021 July 30 from the White Sands Missile Range. With its large $12' \times 33'$ slot, MaGIXS targeted two active regions: 12846 and 12849 (Figure 5 (left)). During flight, the slitjaw context imager was deemed too saturated from scattered light to be used for visual acquisition of the targets, so predetermined coordinates were relied upon. After initial pointing adjustments were made to confirm the lack of real-time targeting capability with the slitjaw, the Solar Pointing Attitude Rocket Control System (SPARCS) maintained a constant target for the duration of the flight. MaGIXS captured 374 total seconds of stable solar viewing data, including the initial repointing period. The final target was observed for 298 s. Postflight analysis revealed an offset between the slot and the optical axis, resulting in significant vignetting of the system. This effect is discussed in detail in Section 4.3.3. The resulting effective field of view (FOV) is shown in Figure 5 (right). The X-ray bright points used for further analysis in the following sections are also highlighted.

The altitude of the sounding rocket as a function of time as determined from White Sands Missile Range radar measurements is shown in Figure 6, with approximate flight event timings overlaid. Table 2 lists the times and positions of the repointings.

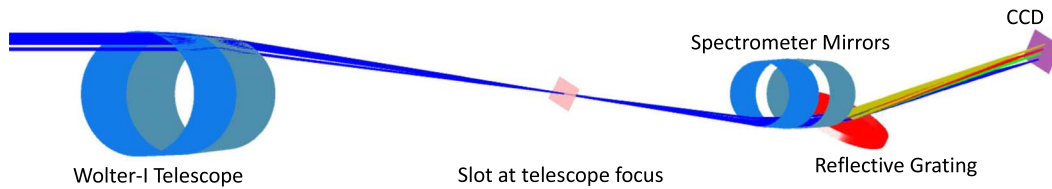


Figure 4. Ray-trace diagram of the MaGIXS optical system.

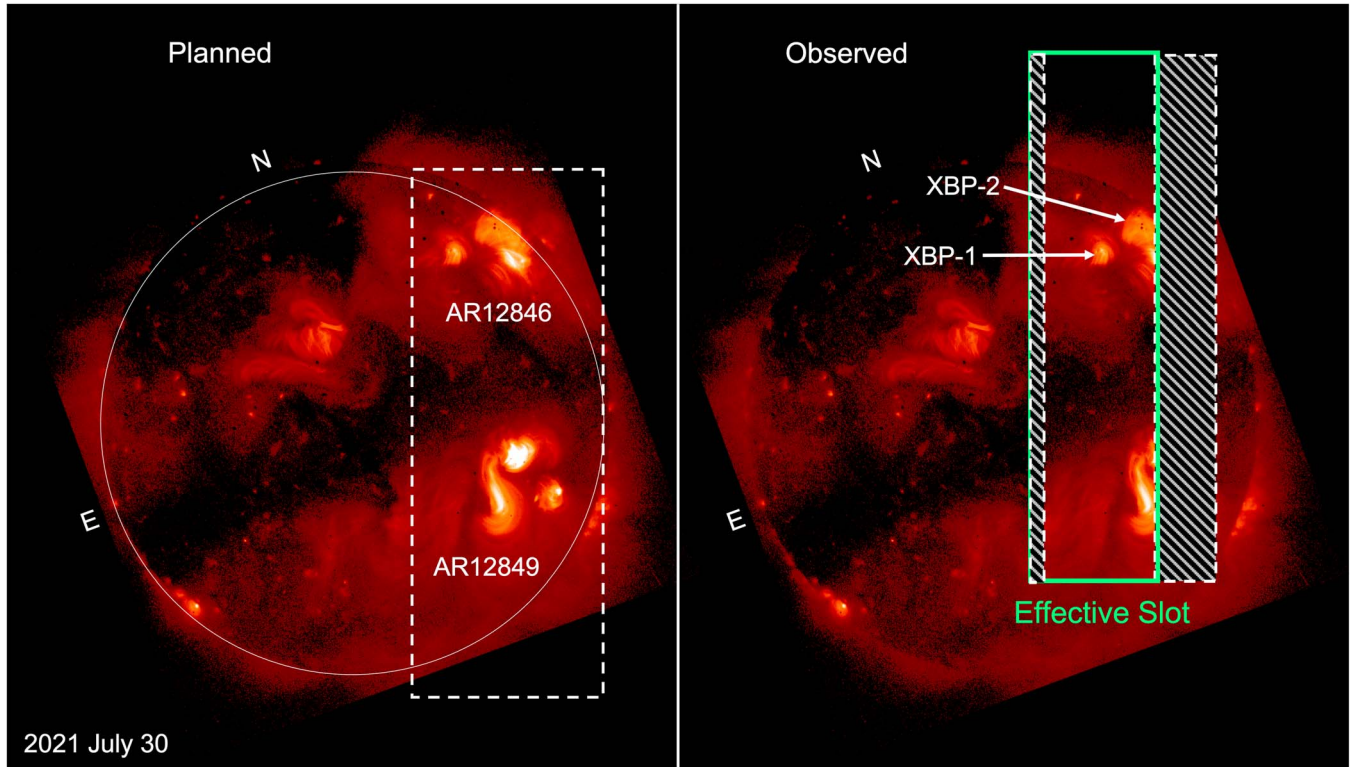


Figure 5. (Left) Planned targeted field of view for flight overlaid on an SXR image from Hinode/XRT (Thin-Be). The MaGIXS slot is indicated by the dashed box. (Right) Approximate final slot position during flight. The effective slot is a consequence of slot misalignment and vignetting (described in Section 4.3.3). Initial analyses performed on the two labeled X-ray bright points are described in Section 6.

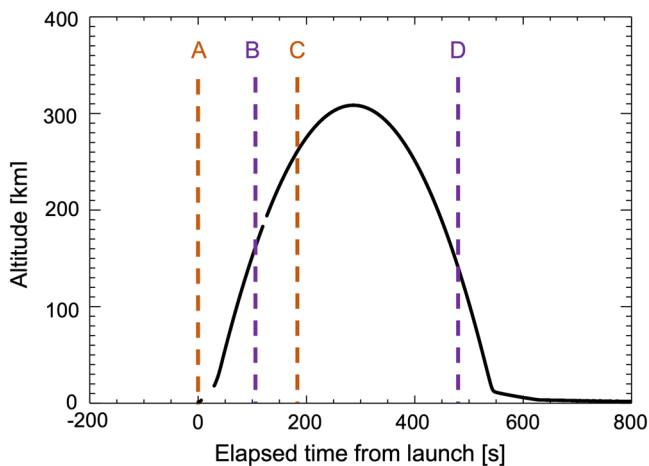


Figure 6. The altitude of the MaGIXS rocket determined from White Sands Missile Range radar data as a function of elapsed time from launch (18:20:00 UT) on 2021 July 30. [A: Launch; B: Stable pointing acquired / First SPARCS pointing; C: Final pointing maneuver; D: Stable pointing ended].

Table 2
SPARCS Pointing Coordinates from Sun Center

Pointing Number	Time Lapsed since Launch s	North arcsec	West arcsec
1	T0+109	527.57	-213.15
2	T0+133	332.0	247.68
3	T0+144	386.63	270.89
4	T0+149	441.30	294.10
5	T0+155	495.98	317.31
6	T0+160	550.65	340.52
7	T0+182	605.33	363.72
8	T0+185	660.00	386.93

4. MaGIXS Data Analysis

4.1. Data Description

All 16-bit images acquired from the MaGIXS science camera were saved on board in the form of FITS files. Images were acquired at a constant 2 s cadence, starting at launch and

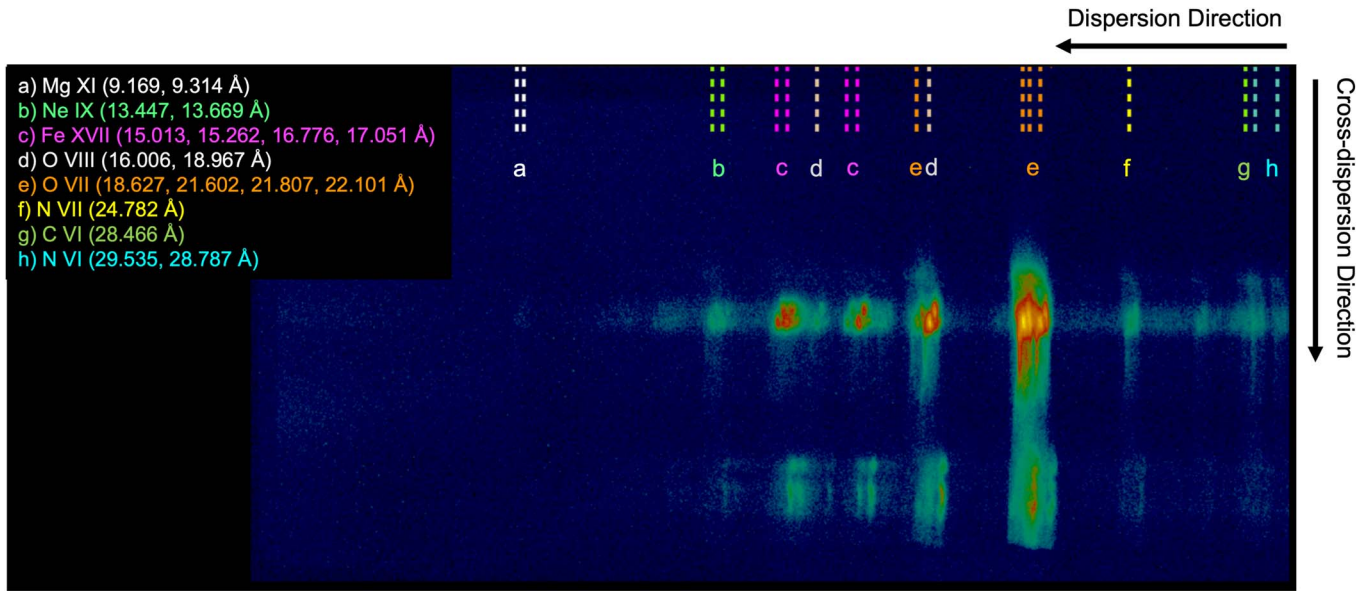


Figure 7. Level 1.5 summed MaGIXS data over the entire flight, with key spectral line positions indicated along the dispersion direction.

ending after the shutter door was closed; the images acquired with the door closed are used as dark frames. Due to the utilization of frame-transfer mode, there was no time gap between images. A total of 254 frames were captured during flight, including 23 dark frames before the shutter door opened, 39 frames during pointing maneuvers, 148 frames at the final stable pointing, and 10 dark frames after the shutter door closed. Each readout register of the detector included 50 Non-Active Pixels (NAPs), which are used to determine the bias.

4.2. Data Processing

Initial image processing of the MaGIXS data includes bias subtraction, dark current subtraction, gain adjustment, bad pixel removal, and despiking.

Bias: The non-active regions of the images are used to determine the bias pedestal, which varies slightly between quadrants and as a function of time. The bias is calculated and removed per frame and per quadrant.

Dark Current: During ascent and descent, dark frames are obtained matching the exposure time of the science images (i.e., the images exposed to sunlight). Due to a continual temperature increase in the analog chain during data collection that causes an increase in dark current, a pre-master dark is created from dark frames on the ascent and a post-master dark is created from dark frames on the descent. The same number of dark frames are used to create the master darks. The averaged analog chain temperature is stored with the associated master dark. To deal with particle hits, any pixel greater than three times the standard deviation of the pixel over the darks is ignored before creating the master dark. Dark current is removed from a science image by creating an interpolation between the pre- and post-master dark using the science image’s analog chain temperature.

Gain: The gain was measured with an Fe-55 source during preflight testing of the MaGIXS camera to be 2.6 electrons per Data Number (DN).

Bad Pixels: Bad pixel maps are created using dark images. Bad pixels are evaluated for each pixel location over the set of dark images. If the values are not within three times the

standard deviation of the mean for at least 80% of the time, the pixel location is marked as bad. Bad pixels are replaced by taking the median of the surrounding pixels. The replaced locations and values are stored in a table with the image.

Despiking: Despiking uses a recursive technique to replace pixels of suspected particle hits. A list is created of pixels over a specified threshold. Pixels with values from lowest to the highest are evaluated to allow for subtraction of radiation hits. Images are divided into areas where individual thresholds can be applied. If a pixel is determined to be replaced, the median of the surrounding pixels is used. The replaced locations and values are stored in a table with the image.

Data sets have been generated for varying levels of processing. Level 0.1 is the bad pixel mask. Level 0.2 contains the pre- and post-master darks. Level 0.5 is the Level 0 image set with time-stamp adjustment applied, image acquisition state defined, and the CCD holder and cold block temperatures included. The image acquisition states are dark, pointing, light, shutter door opening, and shutter door closing. Level 1.0 is processed from the Level 0.5 Sun-exposed (“light”) images with the bias and dark subtracted, the gain adjusted, and the bad pixels corrected. Level 1.5 is the despiked Level 1.0 image set.

4.3. Flight Calibration

For flight calibration, we considered Level 1.5 processed images from stable pointing, which was established 185 s after launch (see Table 2). Figure 7 shows MaGIXS Level 1.5 data summed over 148 frames, which are used for flight calibration.

4.3.1. Spatial Plate Scale

In the cross-dispersion direction, the spatial plate scale is $2''.8 \text{ pixel}^{-1}$. In the dispersion direction, the spatial plate scale varies with both field angle and wavelength, which is a property of the variable line-spaced reflective grating used in MaGIXS. These relationships are demonstrated in Figure 8, derived using an optical model of the grating in Zemax. A table of the average spatial plate scale for key spectral lines is given in Table 3.

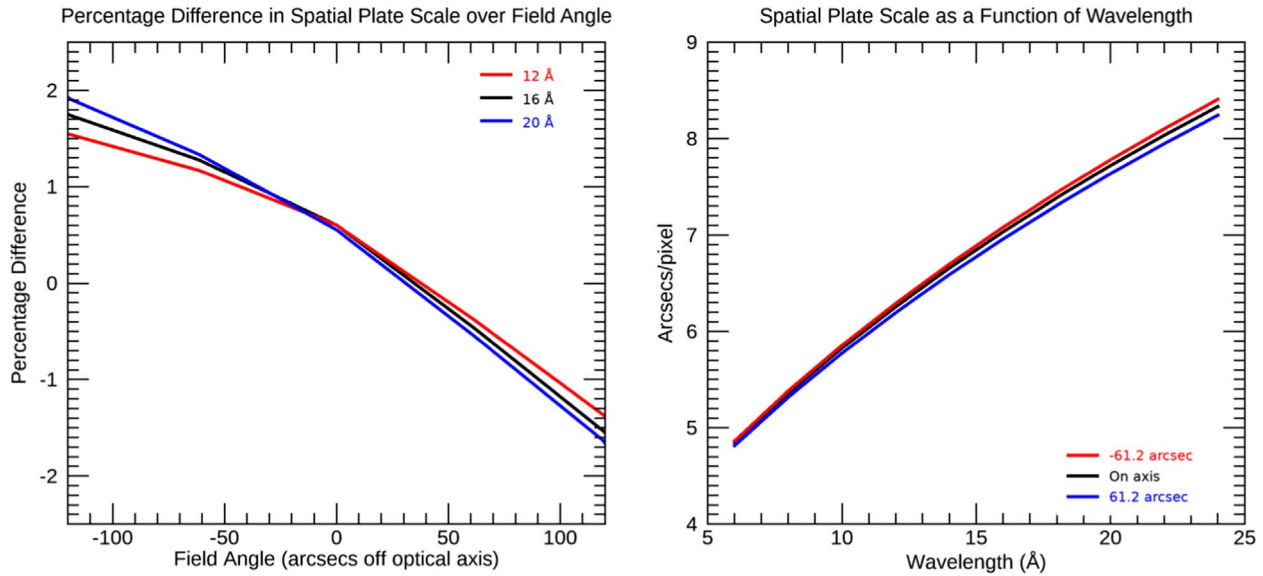


Figure 8. (Left) The spatial plate scale at 16 Å as a function of the field angle from the optical axis. (Right) The plate scale averaged over the field angle as a function of wavelength.

Table 3
Key Spectral Lines and Corresponding Spectral Plate Scale Values

Ion	Wavelength (Å)	Average Plate Scale (" pixel ⁻¹)
N VI	29.535	9.21
N VI	28.787	9.09
C VI	28.466	9.04
N VII	24.782	8.45
O VII	22.101	8.01
O VII	21.602	7.93
O VIII	18.967	7.51
O VII	18.627	7.45
Fe XVII	17.051	7.20
Fe XVII	16.776	7.15
O VIII	16.006	7.00
Fe XVII	15.262	6.86
Fe XVII	15.211	6.85
Fe XVII	15.013	6.81
Ne IX	13.699	6.56
Ne IX	13.447	6.51
Fe XVII	12.124	6.25
Mg XI	9.314	5.60
Mg XI	9.169	5.57

4.3.2. Wavelength Calibration

One critical aspect of analyzing MaGIXS data is to determine the wavelength calibration, meaning the wavelength as a function of pixel value. From ground calibration (see Athiray et al. 2021), we know the relationship is nonlinear and varies as a function of field angle, meaning photons from different locations on the Sun experience different dispersion. Despite completing significant preflight calibration at the X-Ray and Cryogenic Facility (XRCF) at MSFC (Athiray et al. 2021), only the wavelength calibration for a single field angle (“on-axis”) was determined. Additionally, the wavelength calibration shifted between the measurements taken at the XRCF and flight, either due to preflight vibration or 1 g offloading. Hence, the wavelength calibration as a function of field angle must be determined from flight data.

We considered a slice of the MaGIXS spectrum, summed over several rows along the cross-dispersion direction sampling the X-ray bright point-1 (XBP-1) in the northern targeted active region (refer to Figure 5). The resulting spectrum is shown in Figure 9 (left). We identified prominent emission lines in the spectrum and modeled each with a Gaussian function to derive respective centroid pixel locations. We then performed wavelength calibration. Figure 9 (right) shows the wavelength calibration for XBP-1, which is best modeled using a quadratic fit. We define XBP-1 as our reference point and designate it with 0° field angle. This assumption implies the derived wavelength calibration is applicable for the “effective on-axis” (i.e., 0°) field angle. Using these coefficients, we then create a map of wavelength arrays for different field angles using the squashing and spectral plate scale derived from Zemax optical model.

To verify and validate wavelength calibration and the map of wavelength array per field angle, we compared the spatial distance between XBP-1 and XBP-2 from SDO/AIA and MaGIXS images. The spatial separation in the x -direction between XBP-1 and XBP-2 in the rolled solar coordinates determined from the AIA 335 Å image is $\approx 78''$. This value closely matches and is consistent with the distance measured using the flight data ($\sim 70''$ – $78''$), which confirms that the assumed squashing factor derived from Zemax optical model agrees with the derived wavelength calibration.

4.3.3. Roll, Pointing, and Vignetting Function

The roll angle was determined from pointing adjustments made during the first 80 s of flight observation, where the SPARCS was commanded to point to several targets on the Sun such that the instrument was moved along the cross-dispersion direction for 54 s. Table 2 lists the SPARCS pointing coordinates from Sun center, which are marked on the full disk AIA 335 Å image shown in Figure 10 (left). Using the relative offset between these SPARCS pointings, we determined the roll angle to be 23° clockwise about solar north.

During the ground tests, the Lockheed Intermediate Sun Sensor (LISS), an element in SPARCS used for fine pointing,

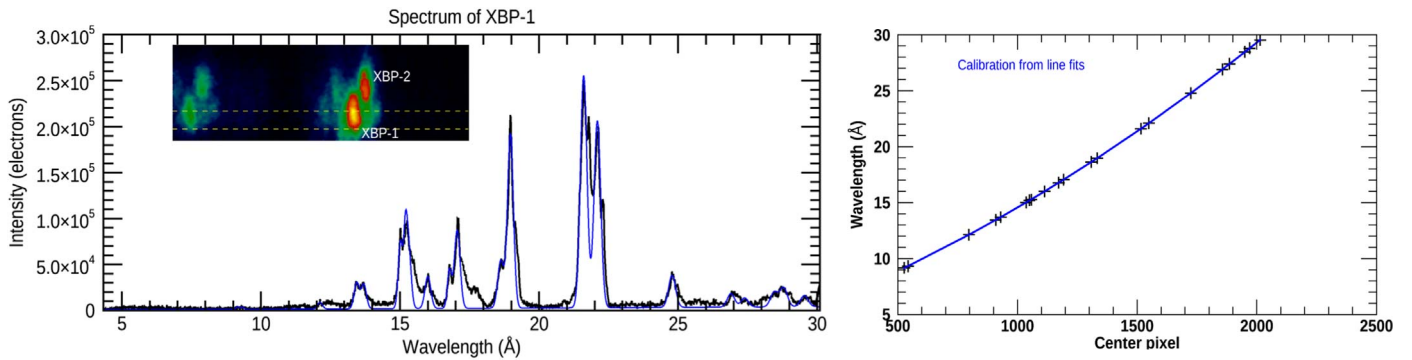


Figure 9. (Left) Spectral profile of XBP-1 derived from slices along the dispersion direction, summed over several cross-dispersion rows. The black curve represents the flight data, while the blue curve is the fit to the bright lines used to determine the centroids. (Right) Wavelength calibration function derived by mapping the centroid positions of the bright XBP-1 lines with position on the detector.

and MaGIXS Wolter-I telescope were coaligned to within $1'$ accuracy using a theodolite and an autocollimator. Despite significant efforts to coalign the MaGIXS optical surfaces, it was discovered during the prelaunch heliostat test at White Sands, just two weeks before launch, that the Wolter-I and the center of the slot were misaligned from the LISS. The measured offset of slot center from LISS determined from the heliostat test was $\sim 6.5 \pm 1'$, which was factored into the preflight pointing calculations.

The offset between the LISS and the alignment of the TMA and SOA could not be accurately determined from the heliostat tests. However, flight data indicate that an offset between the LISS pointing, slot center, and the optical surfaces introduced additional vignetting, which is nontrivial to model. Therefore, we use the flight data combined with optical models with variable offset scenarios to determine appropriate vignetting maps that correspond to the flight observations.

To determine the absolute pointing postflight, we forward modeled MaGIXS observations using a differential emission measure (DEM) map derived from time-averaged coordinated SDO/AIA observations (channels used: 94, 131, 171, 193, 211, and 335 Å), the MaGIXS instrument response, and the vignetting maps for different offset scenarios. We selected pixels around the brightest O VIII emission line at 18.967 Å, used as our reference to compare flight and forward models. The selected MaGIXS image was coaligned with a forward model through cross-correlation techniques, thus determining the optimal offset between the LISS and slot center and defining a plausible vignetting function. Figure 10 shows the most likely absolute solar pointing overlaid with the vignetting map (marked as contours), which forms the “effective slot” ($9.2' \times 25'$). Figure 10 (right) shows the portion of the Sun that reached the MaGIXS grating and science camera.

Consequently, this first MaGIXS flight missed making observations of the brightest portions of the target active regions, due to the significant impact of the slot offset and internal vignetting. However, the measurements taken from the captured portions of the two active regions successfully yielded X-ray spectra, which allow for further analysis, prove the performance of the design, and provide an opportunity to validate the inversion process, as discussed further below.

4.4. Inversion of MaGIXS Data

To unfold the MaGIXS data, we follow the general framework of spectral decomposition described in (Cheung et al. 2015; Winebarger et al. 2019; Cheung et al. 2019) and

described briefly here. We first cast the problem as a set of linear equations, namely

$$y = Mx, \quad (1)$$

where y is a one-dimensional array that contains a single row of the MaGIXS flight data, x is a one-dimensional array of emission measures at different solar locations and temperatures, and M is a matrix that contains how emission at each solar location and temperature map into the detector. The MaGIXS response matrix, M , is generated using the wavelength calibration as a function of field angle determined from flight data and effective area measured preflight (Athiray et al. 2021). Using the CHIANTI atomic database v10.0.2 (Del Zanna et al. 2021b), we construct several variants of isothermal, unit EM instrument response functions with different abundances (i.e., coronal/photospheric), different electron distributions (i.e., Maxwellian/kappa), and an assumption of ionization equilibrium. Equation (1) is then solved for x using the ElasticNet routine in SciPy, a Python library. ElasticNet allows for varying the extent of smoothness and sparseness while finding convergence to the best solution. (Using ElasticNet is a difference from the previous published papers, which used the LassoLars routine.)

The ElasticNet routine is solving Equation (1) by finding

$$x^\# = \operatorname{argmin}[\|y - Mx\|_2^2 + \alpha\rho\|x\|_1 + 0.5\alpha(1 - \rho)\|x\|_2^2], \quad (2)$$

where α is the penalty term and ρ is varied from 0 to 1 (note that α and ρ are unitless minimization parameters and do not represent physical quantities). The first term in Equation (2) is the standard least-squares term that minimizes the difference between the observations and the forward calculated observations. The second term is the L_1 norm of x ; minimizing this term favors a sparse solution. The third term is the L_2 norm of x ; minimizing this term favors a smooth solution. Increasing α increases the weight of the penalty. For $\rho = 1$, the solution will be sparse, while for $\rho = 0$, the solution will be smooth. We inverted the data with a variety of α and ρ solutions, comparing how well the inverted data, Mx , matched the observations, y . We also considered different inversion routines that were purely sparse (such as LassoLars) or purely smooth. We will present the parameter space search and provide a quantitative comparison of different algorithms in a future paper. For the

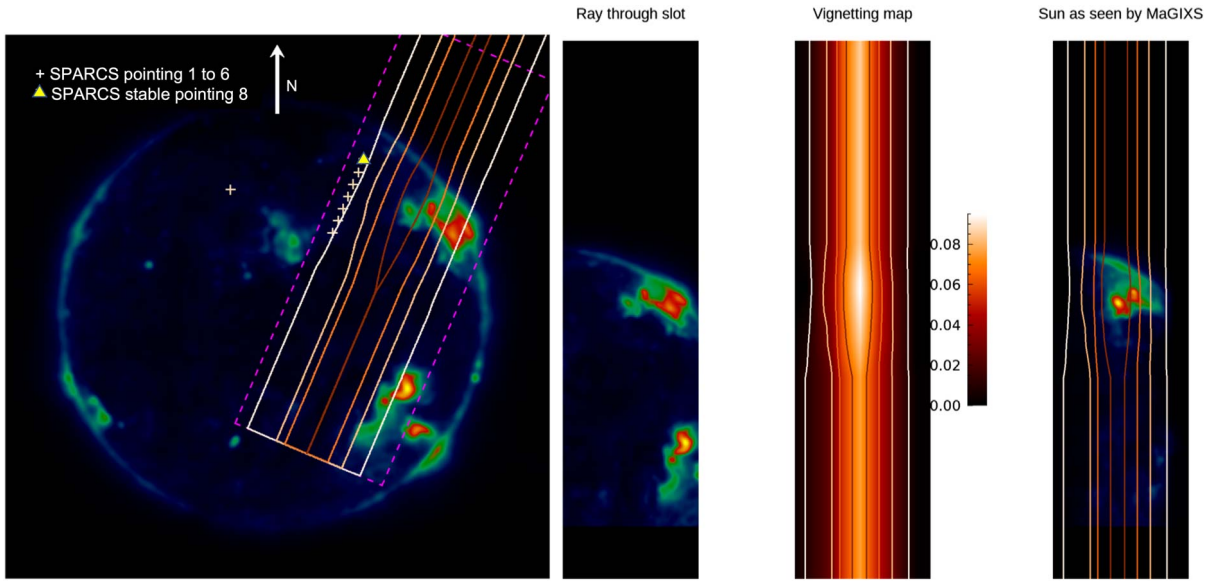


Figure 10. (Left) Vignetting contours (solid) overlaid onto an SDO/AIA 335 Å image. The dashed box indicates the extent of the physical slot. The crosses indicate the SPARCS pointings. (Middle) Derived contoured vignetting map. (Right) Effective slot seen by MaGIXS due to the slot misalignment and optical vignetting.

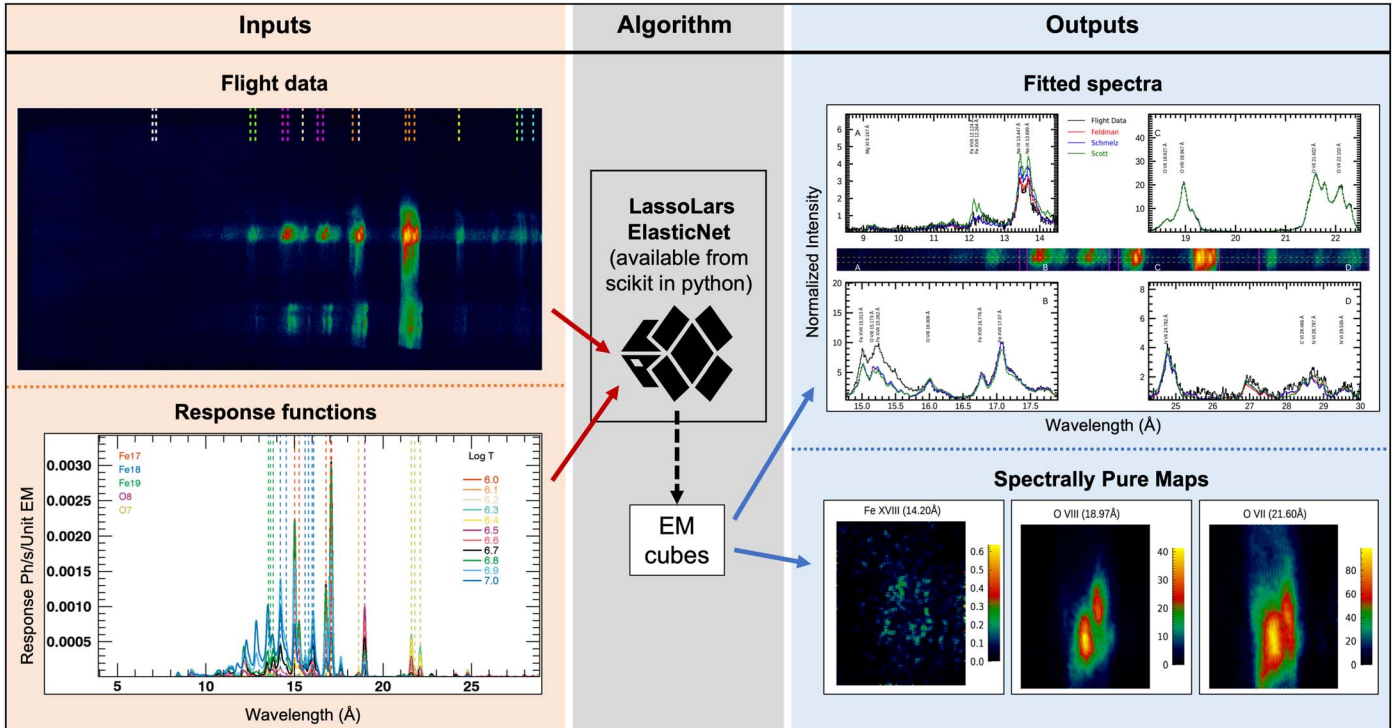


Figure 11. Schematic description of the inversion process of converting a spectroheliogram to pure spectral maps.

Level 2 data included in the initial analysis below, we use $\alpha = 1 \times 10^{-5}$ and $\rho = 0.1$.

Figure 11 provides a high-level schematic of the inversion process, wherein the instrument response function and spectroheliogram data are inputs, and the emission measure cubes, fit spectra, and spectrally pure maps of different ion species are the outputs of the inversion. We perform several inversion runs with different response functions as a varying input. In addition to the field angle-wavelength map and effective area, the response function invokes a combination of atomic parameters involving temperature, electron distribution, and abundances as

listed in Figure 12. All of the responses are constructed under the assumption of ionization equilibrium. Figure 12 (right) shows an example of response functions for an on-axis source for different abundances using a Maxwell electron distribution. We then determine multiple inverted solutions for various possible input combinations and compare the results with the flight fitted spectrum to select the best-matched solution.

4.4.1. Example Inversion

Figure 13 provides an example of the inversion of the XBP-1 spectroheliogram. The inset shows a cropped section of the

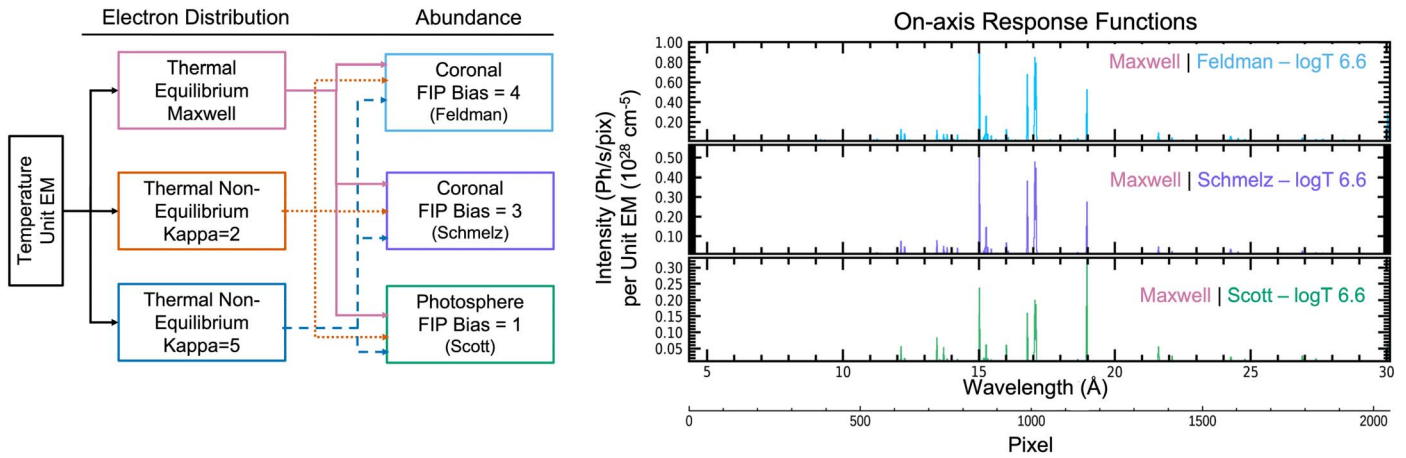


Figure 12. (Left) Depiction of atomic parameter space applied to the generation of the response functions. (Right) Sample response functions for an on-axis source at plasma temperature $\log T = 6.6$. The three panels correspond to response functions for different abundances under Maxwell electron distribution. All of the response functions are generated under the assumption of ionization equilibrium.

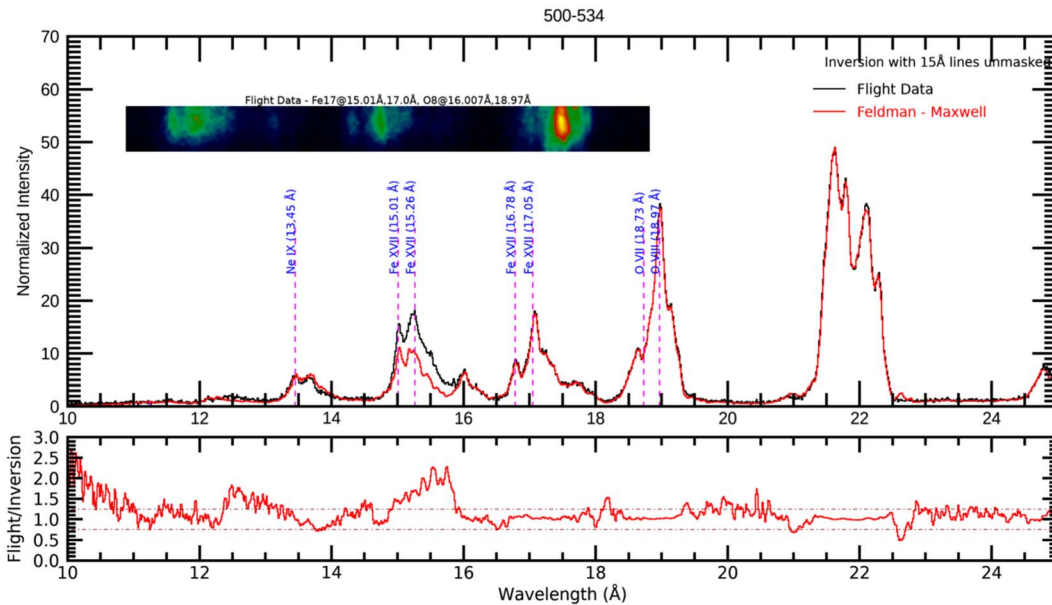


Figure 13. Comparison of flight and inverted spectra using coronal abundances (Feldman 1992) for the XBP-1 region. The inset shows the spectroheliogram. Bottom panel shows the ratio of flight to inversion.

MaGIXS data around the XBP-1 in the 15–20 Å wavelength range. The spectrum, summed over XBP-1, is plotted with a black line. This sample inversion uses a Maxwell electron distribution, ionization equilibrium, and Feldman coronal abundances (Feldman 1992). The fit spectrum from the inversion results are shown as a red line. The fit spectrum near Fe XVII 15 Å, including the collisional 3C line at 15.013 Å and the intercombination 3D line at 15.262 Å, do not agree with the observed flight data. Specifically, the observed flight data shows an excess emission in the wavelength range of ~ 15 –15.7 Å. We found a similar excess of emission in other spatial structures as well, meaning this result is not limited to XBP-1.

4.4.2. Possible Explanations for Excess Emission

We carried out a multipronged investigation to understand and explain this wavelength-dependent discrepancy. First, we considered the possibility that the selected inversion parameters

did not match the solar conditions well. We completed a parameter space study using responses formed assuming different FIP biases and electron distributions, as well as minimization parameters α and ρ . We found no combination of inversion parameters could be used to explain the excess emission.

Next, we considered whether the excess emission could be due to an instrumental artifact. The excess emission is near the absorption edges of the Ni and Ir (near ~ 14.9 Å), materials used in the MaGIXS X-ray mirrors and coatings, which could have impacted the shape and confidence in the derived effective area. However, to match the observed intensity around the ~ 15 –15.7 Å, the effective area would have to be $\sim 60\%$ higher in this narrow wavelength band, while the current effective area matches well for all other emission lines, including the Fe XVII line at 16.776 Å. We acknowledge the lack of effective area measurements across the Ni edge, but we argue that a 60% increase in the effective area in a narrow wavelength range is not physical, considering that the remaining broad wavelength

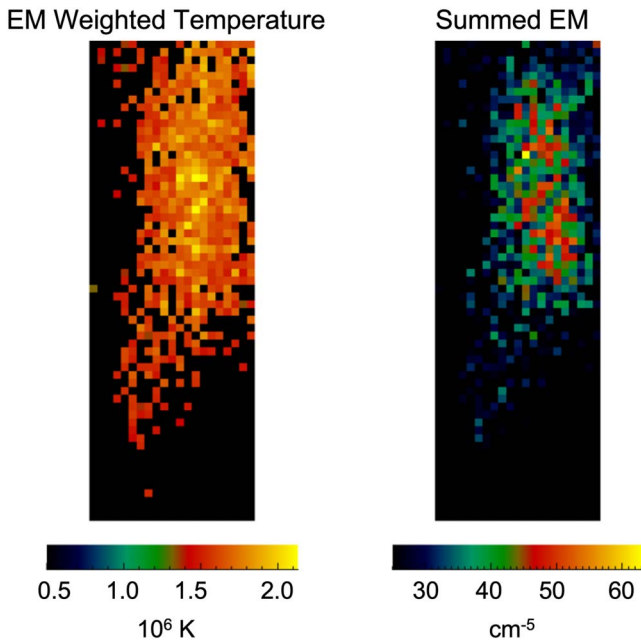


Figure 14. (Left) Emission measure weighted temperature map for XBP-1. (Right) Corresponding summed EM cube.

range agrees with the measured effective area curve (see Athiray et al. 2021).

Finally, we considered the completeness of the atomic database in this wavelength range. We performed a comparison between high-resolution solar spectra and CHIANTI data and found that there are several missing transitions in the database around 15 Å. From analyses of previous solar and laboratory spectra (Beiersdorfer et al. 2012, 2014; Lepson et al. 2017), we know that satellite lines of Fe XVII, Fe XVI, and Fe XV ions are present in this wavelength range. We also know that some are missing in the database, hence they are not included in the response functions. It is well known that a historical discrepancy of the Fe XVII 3C/3D line ratio arises due to the proximity of a satellite line of Fe XVI (15.261 Å) to the Fe XVII 3D line. Recent observations from both EBIT and astrophysical sources indicate that the Fe XVI and Fe XV ions emit a series of emission lines, including several satellite lines, which are blended or are very closely spaced with Fe XVII lines, from 15.01 to 15.7 Å (Brown 2008; Graf et al. 2009).

Generally, in active regions and flares, the satellite lines are much weaker than the Fe XVII lines. The atomic data for the strong Fe XVII lines indicate agreement within 10% with solar high-resolution spectra (Del Zanna 2011), hence the problem cannot be with the atomic data for this ion.

Fe XVI is the simplest ion with only one valence electron in the M shell; Fe XV is the next simplest ion with two valence electrons in the M shell. These ions exhibit peak emissivity near 2 MK. The EM-weighted temperature for the XBP-1 region calculated from an inverted EM cube (see Figure 14) indicates that 2 MK, “relatively cool” plasma emission is dominant. In fact, all the structures in the MaGIXS FOV are relatively cool (with EM-weighted temperatures between 1.5 and 2.5 MK), explaining why the excess of emission is not limited to XBP-1.

The missing flux due to satellite lines would therefore have a significant effect and could explain the excess of emission. Work is in progress to calculate the atomic data and update the

CHIANTI database. In the meantime, given the incompleteness of the atomic data around 15 Å for such low temperatures, we have chosen to remove the 14.5–15.5 Å region from the analysis. The relative variation of the excess emission among the observed structures, including XBP-2, requires further investigation, which is beyond the scope of this paper and will be presented in future results.

4.4.3. Deconvolved Spectral Maps

Plasma diagnostics such as temperature, density, abundances, and electron distribution can be derived from spectroscopic observations by measuring the line intensities and ratios of different spectral lines from different ion species at different ionization states. However, absolute line intensities cannot be directly deduced from spectroheliogram data of an extended source, such as an active regions or X-ray bright point, due to overlapping spatial–spectral information, and therefore need to be inverted to yield spectrally pure maps (as described above in Section 4.4).

One of the primary MaGIXS data products derived from the inversion process is the generation of spectrally pure maps of different observed ion species for the full FOV. These maps are obtained by folding the inverted emission measure cube through the emissivity functions of different ions created using CHIANTI database with the same atomic assumptions (abundances, ionization equilibrium, etc.). Figure 15 shows the spectrally pure maps of XBP-1 and XBP-2 in Fe XVII, Fe XVIII, O VIII, O VII, N VI, and N VII.

5. Coordinated Data

To enhance the science return of the MaGIXS flight, coordinated data sets were specifically obtained from several external solar and astrophysical instruments. These data sets are listed in Table 4, along with continuously available SDO data. It should be noted that, while most of these data sets primarily targeted the brighter southern active region, spatially and temporally overlapping data corresponding to the MaGIXS field of view are available across the solar atmospheric layers. Analyses targeting these coordinated sets will be the subject of forthcoming studies.

6. Discussion

Using the pure spectral maps provided in Figure 15, we have performed targeted analysis of XBP-1. We consider four unique plasma diagnostics signatures, described in Section 1, that contribute to the differentiation between the high- and low-frequency heating scenarios.

I. High-temperature, low-emission plasma: Observing temperature-sensitive diagnostic emission lines such as Fe XVIII and Fe XIX directly indicates the presence of hot plasma, and simple intensity ratios with Fe XVII could help determine the heating frequency. Athiray et al. (2019) showed that line ratios of Fe XVIII and Fe XVII can be directly related to the high-temperature EM slopes (β). The XBP-1 region observed by MaGIXS distinctly emits Fe XVII lines, while little/no significant Fe XVIII emission is observed, as shown in the spectrally pure maps of XBP-1 in Fe XVII and Fe XVIII (Figure 15). Therefore, we cannot strongly infer much about the high-temperature falloff, due to the lack of strong Fe XVIII emission. However, we determine the ratio of Fe XVIII to Fe XVII using the total emission integrated over XBP-1, which

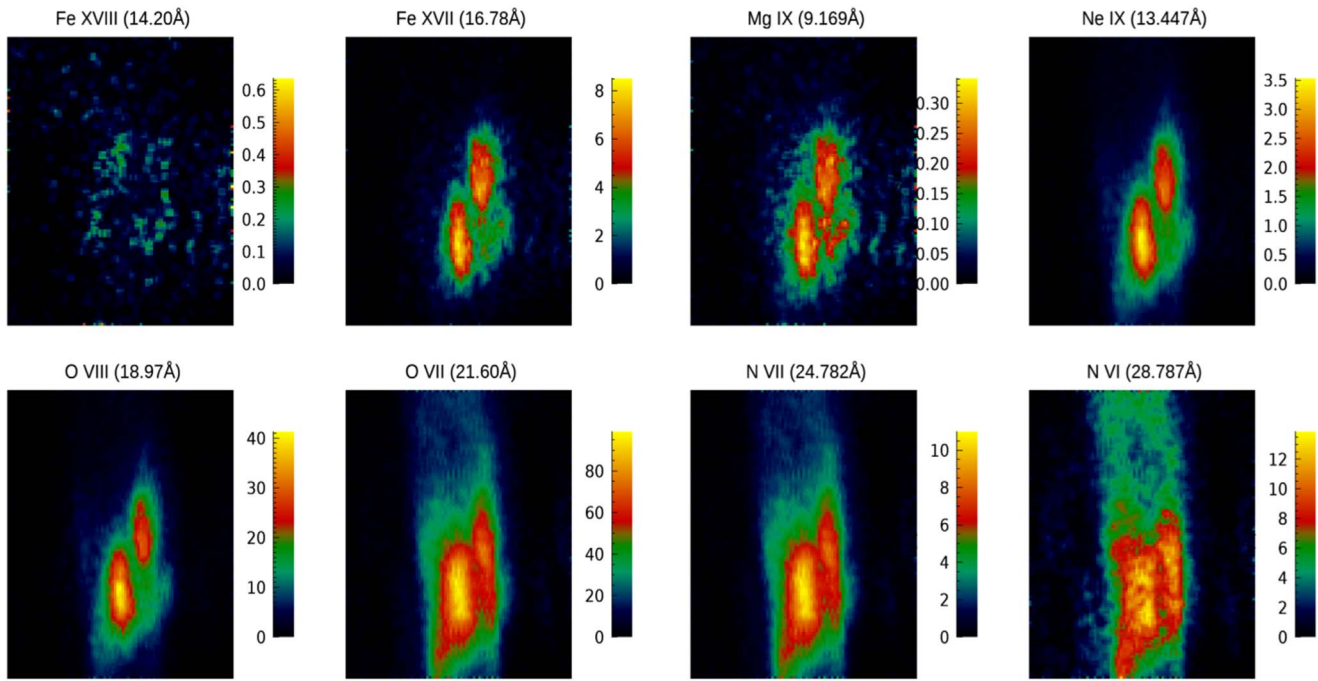


Figure 15. Spectrally pure maps of XBP-1 derived from inversion of the MaGIXS spectroheliogram in units of ph/s/cm^2 .

Table 4

Available Concurrent and Complementary Data Sets Observing at Least One of the MaGIXS Target Regions

Solar Target	Instrument
Photosphere	*Hinode Solar Optical Telescope (SOT) Solar Dynamics Observatory (SDO) Helioseismic and Magnetic Imager (HMI)
Transition Region	SDO Atmospheric Imaging Assembly (AIA) 1600 / 1700 Å
Corona	*Interface Region Imaging Spectrograph (IRIS) SDO AIA short-wavelength EUV Images Hinode EUV Imaging Spectrometer (EIS) Hinode X-Ray Telescope (XRT) Nuclear Spectroscopic Telescope Array (NuSTAR)

Note. *IHOP 421: https://www.isas.jaxa.jp/home/solar/hinode_op/hop.php?hop=0421.

sets an upper limit on the β value for the entire XBP-1 region as shown in Figure 16. The black solid line indicates the ratio of Fe XVIII/Fe XVII as a function of β for a peak temperature at $\log T_{\max} = 6.30$. The observed ratio with uncertainty (0.024 ± 0.003) is denoted by horizontal lines (solid red, dashed blue). The intersection of the horizontal (red) and vertical lines (green) on the plot denote the upper limit for β to the ratio derived from MaGIXS. The range of allowed β values corresponding to the uncertainty in the observed ratio is represented by vertical dashed lines. The low ratio (0.024) suggests high β (6.09), indicating a high-frequency heating scenario for this bright point.

II. Element abundances of high-temperature plasma: Determining the abundances of elements in the solar corona is a primary objective of the MaGIXS instrument. Based on previous analyses, we expected quiescent active region cores to have a FIP bias of 3–4 at the temperatures of the MaGIXS lines [(e.g., Del Zanna & Mason 2014); also refer back to Section 1 (II)]. However, recent line-to-continuum

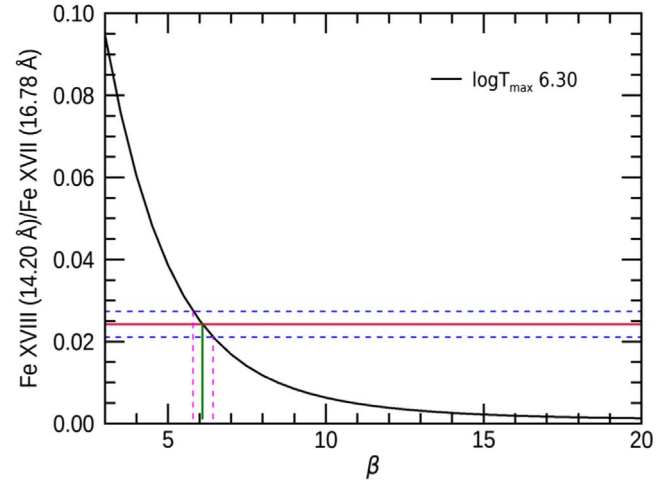


Figure 16. Intensity ratios of Fe XVIII/Fe XVII as a function of EM slope (β) with peak temperature at $\log T_{\max} = 6.30$. With little/no dominant Fe XVIII emission in MaGIXS, the observed ratio for the integrated XBP-1 region (0.024 ± 0.003) serves as an upper limit for β (denoted by the intersection of the solid red horizontal line with the solid green vertical line). The dashed vertical lines denote the range of allowed beta values corresponding to the uncertainty in the observed ratio.

measurements reported by Vadawale et al. (2021) of the full Sun in X-rays have indicated that XBPs have a lower FIP bias, although those measurements were performed with a disk-integrated instrument. To determine which abundance matches the MaGIXS data, we generated several MaGIXS response functions using coronal (Feldman 1992; Schmelz et al. 2012) and photospheric abundances (Scott et al. 2015), as described in Section 4.4. Inversions are performed using different response functions, and the results are compared in Figure 17. The clearest abundance diagnostics in the relatively cool XBP-1 are from the Ne IX lines between 13 and 14 Å, shown in panel A of Figure 17. Specifically, the coronal FIP bias (~ 4) from Feldman (1992) agrees most closely with the

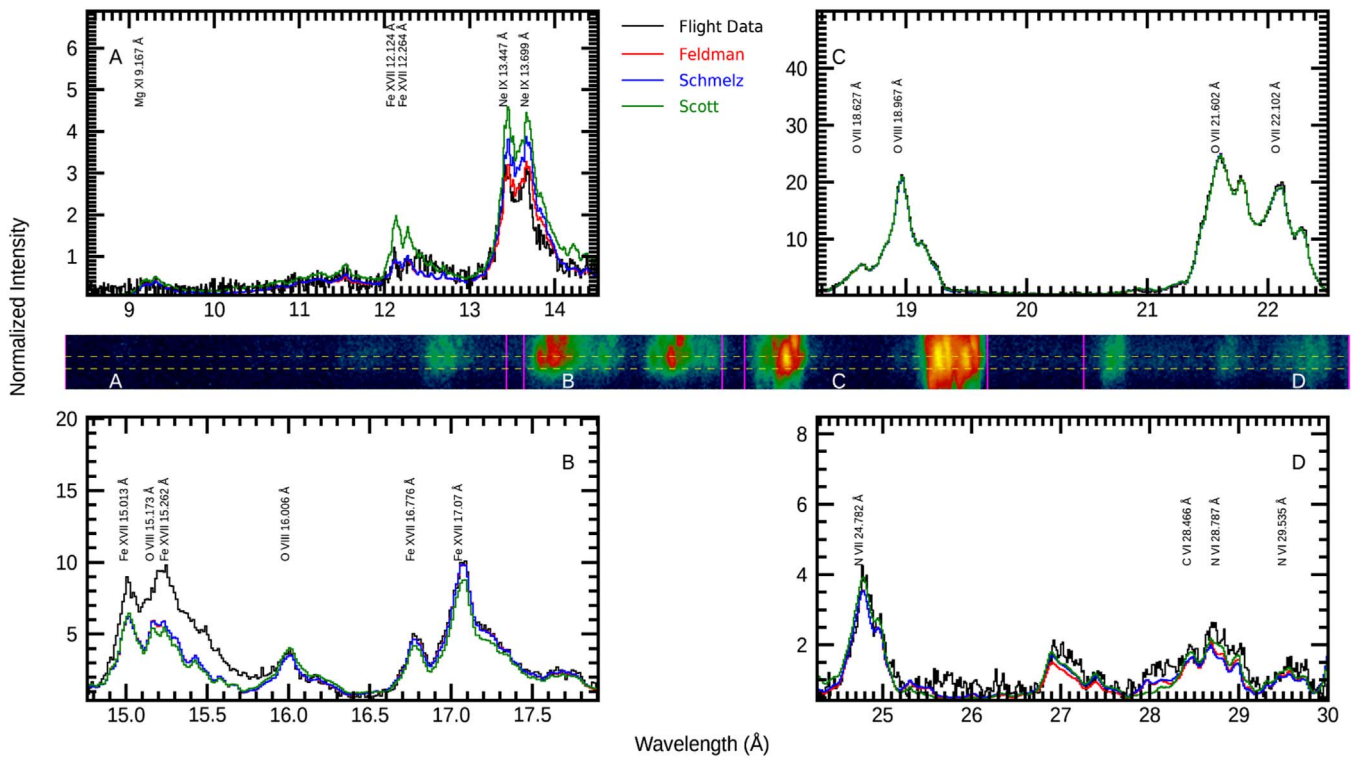


Figure 17. Comparison of flight and inverted spectra using different solar abundances (Coronal - Feldman 1992; Schmelz et al. 2012; Photospheric - Scott et al. 2015) for the XBP-1 region. Top and bottom panels (A), (B), (C), and (D) compare spectra from different wavelength ranges with the prominent emission lines labeled. The cropped flight spectroheliogram is shown in the middle, with the corresponding wavelength ranges marked with vertical lines. Horizontal dashed lines indicate the rows that are summed for the XBP-1 spectra. Note all inversions underestimate the observed emission in the 15–15.7 Å wavelength range, as discussed in Section 4.4.2.

flight data. Note that the observed Ne lines are reproduced consistently by the Feldman model, whereas the Schmelz model overpredicts the measurements.

III. Temporal variability of high-temperature plasma: The fluctuations of Fe XVII line intensities with time probes the impulsiveness of heating events. The emissivity of Fe XVII peaks at ~ 3 –5 MK, near the peak emission from a typical active region. Small-scale heating events would result in temporal fluctuations of the intensity of Fe XVII emission. To generate light curves of the Fe XVII intensity from the MaGIXS data, we sum every 4 frames of the 148 frames of MaGIXS flight data to build sufficient statistics, resulting in 144 spectroheliograms, each with an effective exposure time of 8 s. We then perform an inversion for each spectroheliogram and derive Level 2.0 spectrally pure maps. Figure 18 shows the light curve of Fe XVII for the XBP-1 region. We observe steady intensity of Fe XVII emission over the entire MaGIXS flight with no sudden brightness or variations observed in the light curve. This temporal stability implies that the XBP-1 did not encounter any sudden burst of impulsive energy release to heat the ambient plasma during the MaGIXS observations.

IV. Presence of non-Maxwellian electron distributions: The non-Maxwellian κ -distribution contains Maxwellian core electrons and high-energy power-law tail. Dudik et al. (2019) demonstrated that numerous Fe XVII and Fe XVIII lines within the MaGIXS wavelength range are sensitive to κ and can serve as spectral diagnostic for non-Maxwellian electrons. To study this, we first created a MaGIXS response function with κ distributions using a κ database (Dzifčáková et al. 2015; Dzifčáková et al. 2021) assuming coronal abundances (Feldman 1992). We then performed an inversion on the MaGIXS data,

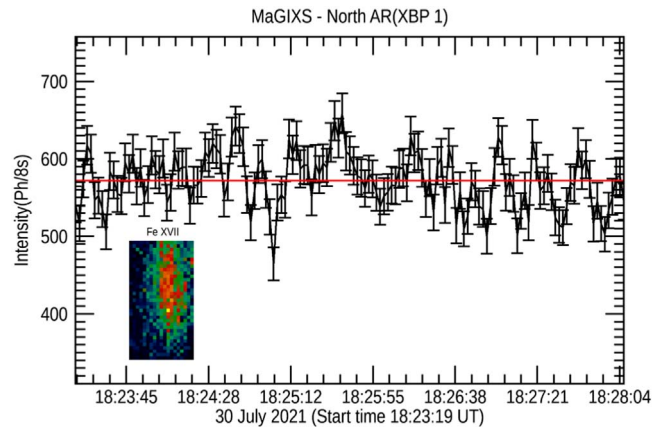


Figure 18. Light curve of Fe XVII emission from XBP-1 constructed by inverting the running averaged data with four frames added at each time bin. Error bars are from photon noise only and are 1σ . Red line is the average intensity.

solving for T and EM for different κ values. For illustration, we considered inversions for $\kappa = 2$ and 5, respectively.

Figure 19 shows the inverted spectroheliogram spectra for different κ values, which indicates that the inversion with the κ distributions does not match flight observations. Note also that an increase in κ results in a closer match between the strong lines and the flight data, supporting the notion that increasing κ approaches a Maxwellian electron distribution. Interestingly, we also observe that invoking a κ distribution predicts many diagnostic emission lines that are not observed in the flight data, which could be a useful diagnostic for future flights. From

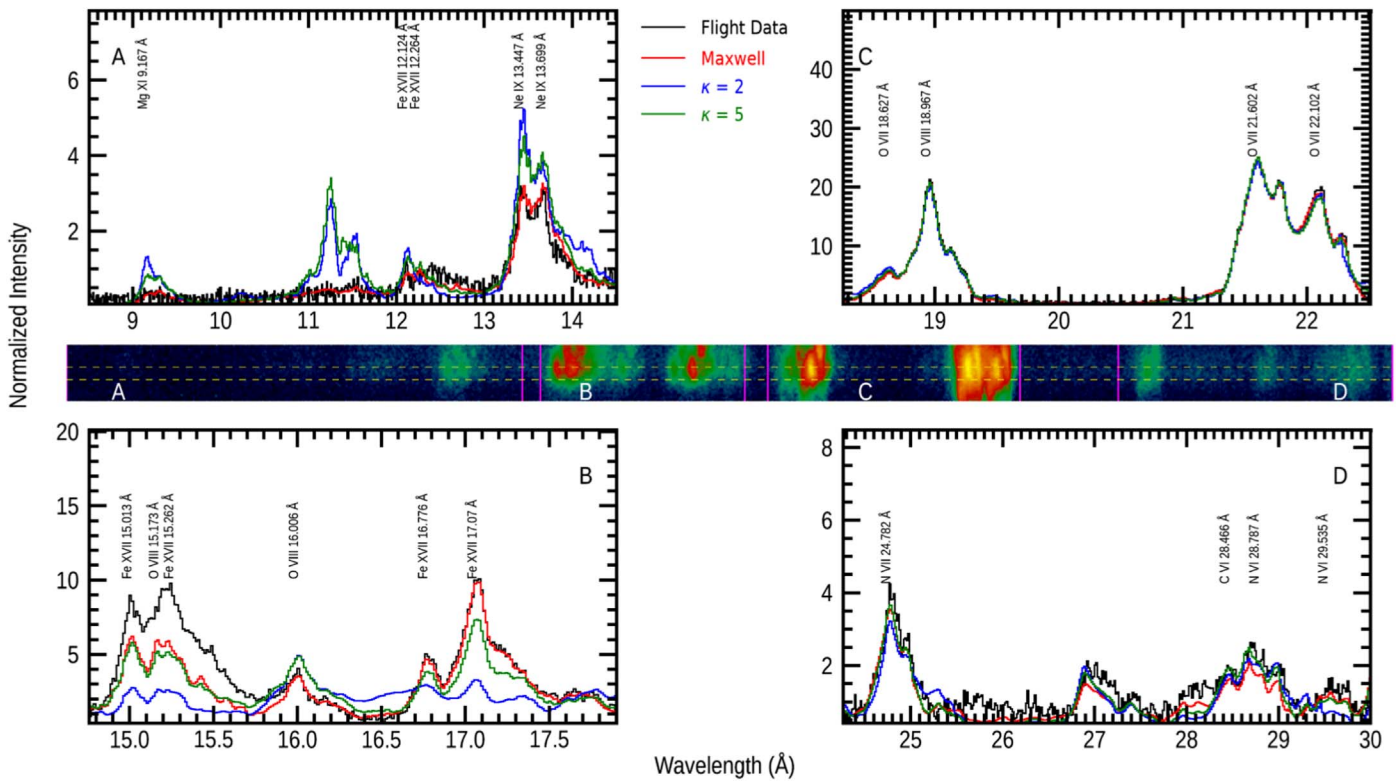


Figure 19. Comparison of flight and inverted spectra using Maxwellian and $\kappa = 2$ and $\kappa = 5$ electron distributions for the XBP-1 region. Top and bottom panels (A), (B), (C), and (D) compare spectra from different wavelength ranges with the prominent emission lines labeled. The cropped flight spectroheliogram is shown in the middle, with the corresponding wavelength ranges marked with vertical lines. Horizontal dashed lines indicate the rows that are summed for the XBP-1 spectra.

these analyses, we infer that the XBP-1 under study is dominated with thermal electrons with no significant non-thermal electrons, strongly suggesting that the XBP-1 region is in thermal equilibrium.

7. Conclusions

Despite the technical challenges encountered during this first flight of the MaGIXS sounding rocket experiment that resulted in less-than-ideal pointing, the soft X-ray spectral images of coronal activity captured and the spectrally pure maps subsequently produced represent a revolutionary breakthrough in the field of high-energy spectral imaging.

Even with the brevity of the flight and the lack of primary target observations from vignetting, MaGIXS still made a key discovery—namely, the presence of excess emission in the 15–15.7 Å wavelength range due to unmodeled Fe XVI satellite lines. Based on the analysis presented in Section 4.4.2, exploring possible explanations for the excess emission discrepancy, and upon further review of the emission lines near the 15 Å region through consultation with atomic experts, the MaGIXS team is reasonably confident that the observed excess emission is chiefly dominated by unmodeled emission lines, in particular missing flux due to transitions from Fe XVI autoionizing states. Dominant, relatively cool (2 MK) plasma, which we observe in both X-ray bright point regions, is expected to produce relatively bright emission from the satellite lines, which enhances the emission near 15 Å, as is observed. This enhancement is consistent with the understanding that satellite line intensities will vary significantly at lower temperatures (see, for example, Del Zanna & Mason 2018). Preliminary calculations indicate an increase in total flux from

Fe XVI and Fe XVII at 2 MK in the 14.9–15.7 Å range by a factor of 1.8 (Del Zanna, private communication). Better understanding of the relative intensities of these lines requires updating the Chianti database through benchmarking the atomic database for low-temperature plasma at these wavelengths as well as significantly improving the spectral resolution of X-ray instrumentation.

By serendipitous virtue of observing the soft X-ray spectra of relatively cool temperature structures on the Sun (in a wavelength range that the Chandra High Energy Transmission Grating has been targeting astrophysical sources with for over 20 yr), MaGIXS discovered the importance of several emission lines currently missing from the Chianti atomic physics database.

The MaGIXS data have also been shown here to address the mission objectives related to coronal heating by focusing on an X-ray bright point region beyond the active region core (XBP-1). (1) The high-temperature emission measure slopes indicate that the region experiences high-frequency (e.g., wave) heating. (2) The bright point abundance diagnostics agree with a coronal FIP bias, similar to quiescent active region cores, and are consistently reproduced by the Feldman model. (3) The lack of impulsive energy release detection in the X-ray light curve during the observations implies steady heating, at least during the duration of the flight. (4) Finally, the close agreement between the inverted spectroheliogram spectra with a Maxwellian electron distribution strongly suggests that this region is in thermal equilibrium.

A reflight of the MaGIXS instrument, with a modified configuration significantly reducing the impact of alignment tolerances, is in preparation for capturing observations of an

active region core. These first results demonstrate that SXR spectral imaging can be a powerful tool in discriminating heating frequency within different coronal structures, paving the way for mapping coronal heating sources across the Sun.

We acknowledge the Marshall Grazing Incidence X-ray Spectrometer (MaGIXS) instrument team for making the data available through the 2014 NASA Heliophysics Technology and Instrument Development for Science (HTIDS) Low Cost Access to Space (LCAS) program, funded via grant NNM15AA15C. MSFC/NASA led the mission, with partners including the Smithsonian Astrophysical Observatory, the University of Central Lancashire, and the Massachusetts Institute of Technology. MaGIXS was launched from the White Sands Missile Range on 2021 July 30. The MaGIXS team gratefully acknowledges the Hinode and IRIS (IHOP 421), NuSTAR, and SDO missions for providing coordinated observations during the launch. J.D. acknowledges project No. 22-07155S of the Grant Agency of the Czech Republic as well as institutional support RVO: 67985815 from the Czech Academy of Sciences. The MaGIXS team would also like to acknowledge the helpful comments from an anonymous reviewer.

ORCID iDs

Sabrina L. Savage  <https://orcid.org/0000-0002-6172-0517>
 Amy R. Winebarger  <https://orcid.org/0000-0002-5608-531X>
 Ken Kobayashi  <https://orcid.org/0000-0003-1057-7113>
 P. S. Athiray  <https://orcid.org/0000-0002-4454-147X>
 Leon Golub  <https://orcid.org/0000-0001-9638-3082>
 Robert W. Walsh  <https://orcid.org/0000-0002-1025-9863>
 Stephen Bradshaw  <https://orcid.org/0000-0002-3300-6041>
 Alexander R. Brucoleri  <https://orcid.org/0000-0001-5927-3300>
 Patrick R. Champey  <https://orcid.org/0000-0002-7139-6191>
 Edward E. DeLuca  <https://orcid.org/0000-0001-7416-2895>
 Giulio Del Zanna  <https://orcid.org/0000-0002-4125-0204>
 Jaroslav Dudík  <https://orcid.org/0000-0003-1308-7427>
 Ralf K. Heilmann  <https://orcid.org/0000-0001-9980-5295>
 Edward Hertz  <https://orcid.org/0000-0002-6747-9648>
 Chad Madsen  <https://orcid.org/0000-0001-8775-913X>
 Helen Mason  <https://orcid.org/0000-0002-6418-7914>
 David E. McKenzie  <https://orcid.org/0000-0002-9921-7757>
 Katharine K. Reeves  <https://orcid.org/0000-0002-6903-6832>
 Mark L. Schattenburg  <https://orcid.org/0000-0001-6932-2612>
 Paola Testa  <https://orcid.org/0000-0002-0405-0668>
 Genevieve D. Vigil  <https://orcid.org/0000-0002-7219-1526>
 Harry P. Warren  <https://orcid.org/0000-0001-6102-6851>

References

- Asgari-Targhi, M., & van Ballegooijen, A. A. 2012, *ApJ*, 746, 81
 Athiray, P. S., Vievering, J., Glesener, L., et al. 2020, *ApJ*, 891, 78
 Athiray, P. S., Winebarger, A. R., Barnes, W. T., et al. 2019, *ApJ*, 884, 24
 Athiray, P. S., Winebarger, A. R., Champey, P., et al. 2021, *ApJ*, 922, 65
 Barnes, W. T., Bradshaw, S. J., & Viall, N. M. 2019, *ApJ*, 880, 56
 Barnes, W. T., Bradshaw, S. J., & Viall, N. M. 2021, *ApJ*, 919, 132
 Barnes, W. T., Cargill, P. J., & Bradshaw, S. J. 2016, *ApJ*, 829, 31
 Beiersdorfer, P., Bode, M. P., Ishikawa, Y., & Diaz, F. 2014, *ApJ*, 793, 99
 Beiersdorfer, P., Diaz, F., & Ishikawa, Y. 2012, *ApJ*, 745, 167
 Bradshaw, S. J., & Viall, N. M. 2016, *ApJ*, 821, 63
 Brooks, D. H. 2019, *ApJ*, 873, 26
 Brooks, D. H., Baker, D., van Driel-Gesztelyi, L., & Warren, H. P. 2017, *NatCo*, 8, 183
 Brooks, D. H., Warren, H. P., & Ugarte-Urra, I. 2012, *ApJL*, 755, L33
 Brosius, J. W., Daw, A. N., & Rabin, D. M. 2014, *ApJ*, 790, 112
 Brown, G. V. 2008, *CaPh*, 86, 199
 Cargill, P. J. 2014, *ApJ*, 784, 49
 Champey, P. R., Winebarger, A. R., Kobayashi, K., et al. 2022, *JAI*, 11, 2250010
 Cheung, M. C. M., Boerner, P., Schrijver, C. J., et al. 2015, *ApJ*, 807, 143
 Cheung, M. C. M., De Pontieu, B., Martinez-Sykora, J., et al. 2019, *ApJ*, 882, 13
 Chitta, L. P., Peter, H., & Young, P. R. 2016, *A&A*, 587, A20
 Del Zanna, G. 2011, *A&A*, 536, A59
 Del Zanna, G., Andretta, V., Cargill, P. J., et al. 2021a, *FrASS*, 8, 33
 Del Zanna, G., Dere, K. P., Young, P. R., & Landi, E. 2021b, *ApJ*, 909, 38
 Del Zanna, G., & Ishikawa, Y. 2009, *A&A*, 508, 1517
 Del Zanna, G., & Mason, H. E. 2014, *A&A*, 565, A14
 Del Zanna, G., & Mason, H. E. 2018, *LRSP*, 15, 5
 Del Zanna, G., Mitra-Kraev, U., Bradshaw, S. J., Mason, H. E., & Asai, A. 2011, *A&A*, 526, A1
 Drake, J. J., & Testa, P. 2005, *Natur*, 436, 525
 Dudík, J., Del Zanna, G., Rybák, J., et al. 2021, *ApJ*, 906, 118
 Dudík, J., Džifčáková, E., Del Zanna, G., et al. 2019, *A&A*, 626, A88
 Džifčáková, E., Dudík, J., Kotrč, P., Fárnik, F., & Zemanová, A. 2015, *ApJS*, 217, 14
 Džifčáková, E., Dudík, J., Zemanová, A., Lörinčík, J., & Karlický, M. 2021, *ApJS*, 257, 62
 Evans, K., & Pounds, K. A. 1968, *ApJ*, 152, 319
 Feldman, U. 1992, *PhysS*, 46, 202
 Golub, L., DeLuca, E., Austin, G., et al. 2007, *SoPh*, 243, 63
 Graf, A., Beiersdorfer, P., Brown, G. V., & Gu, M. F. 2009, *ApJ*, 695, 818
 Guennou, C., Auchère, F., Klimchuk, J. A., Bocchialini, K., & Parenti, S. 2013, *ApJ*, 774, 31
 Gupta, G. R., Tripathi, D., & Mason, H. E. 2015, *ApJ*, 800, 140
 Huenemoerder, D. P., Schulz, N. S., Testa, P., Kesich, A., & Canizares, C. R. 2009, *ApJ*, 707, 942
 Ishikawa, S.-n., Glesener, L., Christe, S., et al. 2014, *PASJ*, 66, S15
 Klimchuk, J. A. 2009, in ASP Conf. Ser. 415, The Second Hinode Science Meeting: Beyond Discovery-Toward Understanding, ed. B. Lites et al. (San Francisco, CA: ASP), 221
 Ko, Y.-K., Doschek, G. A., Warren, H. P., & Young, P. R. 2009, *ApJ*, 697, 1956
 Kobelski, A. R., McKenzie, D. E., & Donachie, M. 2014, *ApJ*, 786, 82
 Laming, J. M. 2015, *LRSP*, 12, 2
 Lepson, J. K., Beiersdorfer, P., Hell, N., et al. 2017, *NIMPB*, 408, 110
 López Fuentes, M. C., & Klimchuk, J. A. 2010, *ApJ*, 719, 591
 McTiernan, J. M. 2009, *ApJ*, 697, 94
 Meyer, J.-P. 1985, *ApJS*, 57, 151
 Miceli, M., Reale, F., Gburek, S., et al. 2012, *A&A*, 544, A139
 Parenti, S., del Zanna, G., Petralia, A., et al. 2017, *ApJ*, 846, 25
 Parker, E. N. 1983a, *ApJ*, 264, 635
 Parker, E. N. 1983b, *ApJ*, 264, 642
 Parkinson, J. H. 1977, *A&A*, 57, 185
 Petralia, A., Reale, F., Testa, P., & Del Zanna, G. 2014, *A&A*, 564, A3
 Raymond, J. C., Kohl, J. L., Noci, G., et al. 1997, *SoPh*, 175, 645
 Reale, F., Parenti, S., Reeves, K. K., et al. 2007, *Sci*, 318, 1582
 Reale, F., Testa, P., Klimchuk, J. A., & Parenti, S. 2009, *ApJ*, 698, 756
 Reale, F., Testa, P., Petralia, A., & Graham, D. R. 2019, *ApJ*, 882, 7
 Schmelz, J. T., Reames, D. V., von Steiger, R., & Basu, S. 2012, *ApJ*, 755, 33
 Scott, P., Grevesse, N., Asplund, M., et al. 2015, *A&A*, 573, A25
 Stansby, D., Baker, D., Brooks, D. H., & Owen, C. J. 2020, *A&A*, 640, A28
 Sylwester, B., Sylwester, J., & Phillips, K. J. H. 2010, *A&A*, 514, A82
 Terzo, S., Reale, F., Miceli, M., et al. 2011, *ApJ*, 736, 111
 Testa, P. 2010, *SSRv*, 157, 37
 Testa, P., & Reale, F. 2012, *ApJL*, 750, L10
 Testa, P., & Reale, F. 2020, *ApJ*, 902, 31
 Testa, P., Reale, F., Landi, E., DeLuca, E. E., & Kashyap, V. 2011, *ApJ*, 728, 30
 Tripathi, D., Mason, H. E., Dwivedi, B. N., del Zanna, G., & Young, P. R. 2009, *ApJ*, 694, 1256
 Tripathi, D., Mason, H. E., & Klimchuk, J. A. 2010, *ApJ*, 723, 713
 Ugarte-Urra, I., & Warren, H. P. 2012, *ApJ*, 761, 21
 Ugarte-Urra, I., & Warren, H. P. 2014, *ApJ*, 783, 12
 Vadawale, S. V., Mondal, B., Mithun, N. P. S., et al. 2021, *ApJL*, 912, L12

- van Ballegoijen, A. A., Asgari-Targhi, M., & Berger, M. A. 2014, [ApJ](#), **787**, 87
- van Ballegoijen, A. A., Asgari-Targhi, M., Cranmer, S. R., & DeLuca, E. E. 2011, [ApJ](#), **736**, 3
- Veck, N. J., & Parkinson, J. H. 1981, [MNRAS](#), **197**, 41
- Vigil, G. D., Winebarger, A. R., Kobayashi, K., et al. 2021, [SoPh](#), **296**, 90
- Warren, H. P. 2014, [ApJL](#), **786**, L2
- Warren, H. P., Winebarger, A. R., & Brooks, D. H. 2012, [ApJ](#), **759**, 141
- Watanabe, T., Hara, H., Yamamoto, N., et al. 2009, [ApJ](#), **692**, 1294
- Widing, K. G., & Sandlin, G. D. 1968, [ApJ](#), **152**, 545
- Williams, T., Walsh, R. W., Peter, H., & Winebarger, A. R. 2020, [ApJ](#), **902**, 90
- Winebarger, A. R., Warren, H. P., Schmelz, J. T., et al. 2012, [ApJL](#), **746**, L17
- Winebarger, A. R., Weber, M., Bethge, C., et al. 2019, [ApJ](#), **882**, 12
- Withbroe, G. L. 1975, [SoPh](#), **45**, 301
- Young, P. R. 2021, [FrASS](#), **8**, 50
- Young, P. R., Watanabe, T., Hara, H., & Mariska, J. T. 2009, [A&A](#), **495**, 587